

REPORT DOCUMENTATION PAGE			Form Approved OMB NO. 0704-0188		
<p>The public reporting burden for this collection of information is estimated to average 1 hour per response, including the time for reviewing instructions, searching existing data sources, gathering and maintaining the data needed, and completing and reviewing the collection of information. Send comments regarding this burden estimate or any other aspect of this collection of information, including suggestions for reducing this burden, to Washington Headquarters Services, Directorate for Information Operations and Reports, 1215 Jefferson Davis Highway, Suite 1204, Arlington VA, 22202-4302. Respondents should be aware that notwithstanding any other provision of law, no person shall be subject to any penalty for failing to comply with a collection of information if it does not display a currently valid OMB control number.</p> <p>PLEASE DO NOT RETURN YOUR FORM TO THE ABOVE ADDRESS.</p>					
1. REPORT DATE (DD-MM-YYYY)		2. REPORT TYPE New Reprint		3. DATES COVERED (From - To) -	
4. TITLE AND SUBTITLE Interfacing whispering-gallery microresonators and free space light with cavity enhanced Rayleigh scattering			5a. CONTRACT NUMBER W911NF-12-1-0026		
			5b. GRANT NUMBER		
			5c. PROGRAM ELEMENT NUMBER 611103		
6. AUTHORS Jiangang Zhu, Sahin K. Özdemir, Huzeyfe Yilmaz, Bo Peng, Mark Dong, Matthew Tomes, Tal Carmon, Lan Yang			5d. PROJECT NUMBER		
			5e. TASK NUMBER		
			5f. WORK UNIT NUMBER		
7. PERFORMING ORGANIZATION NAMES AND ADDRESSES Washington University Campus Box 1054 One Brookings Drive St. Louis, MO 63130 -4862			8. PERFORMING ORGANIZATION REPORT NUMBER		
9. SPONSORING/MONITORING AGENCY NAME(S) AND ADDRESS (ES) U.S. Army Research Office P.O. Box 12211 Research Triangle Park, NC 27709-2211			10. SPONSOR/MONITOR'S ACRONYM(S) ARO		
			11. SPONSOR/MONITOR'S REPORT NUMBER(S) 58381-EL-PCS.16		
12. DISTRIBUTION AVAILABILITY STATEMENT Approved for public release; distribution is unlimited.					
13. SUPPLEMENTARY NOTES The views, opinions and/or findings contained in this report are those of the author(s) and should not be construed as an official Department of the Army position, policy or decision, unless so designated by other documentation.					
14. ABSTRACT Whispering gallery mode resonators (WGMRs) take advantage of strong light confinement and long photon lifetime for applications in sensing, optomechanics, microlasers and quantum optics. However, their rotational symmetry and low radiation loss impede energy exchange between WGMs and the surrounding. As a result, free-space coupling of light into and from WGMRs is very challenging. In previous schemes, resonators are intentionally deformed to break circular symmetry to enable free-space coupling of carefully aligned focused light, which comes with bulky size and alignment issues that hinder the realization of compact WGMR applications.					
15. SUBJECT TERMS monolithic microresonator; silica microspheres; microlasers, fiber taper, microcavities; resonators; light harvesting; nanoparticle; Rayleigh scattering; whispering-gallery-mode; Raman lasing; rare-earth ions					
16. SECURITY CLASSIFICATION OF:			17. LIMITATION OF ABSTRACT UU	15. NUMBER OF PAGES	19a. NAME OF RESPONSIBLE PERSON Lan Yang
a. REPORT UU	b. ABSTRACT UU	c. THIS PAGE UU			19b. TELEPHONE NUMBER 314-935-9543

Report Title

Interfacing whispering-gallery microresonators and free space light with cavity enhanced Rayleigh scattering

ABSTRACT

Whispering gallery mode resonators (WGMRs) take advantage of strong light confinement and long photon lifetime for applications in sensing, optomechanics, microlasers and quantum optics. However, their rotational symmetry and low radiation loss impede energy exchange between WGMs and the surrounding. As a result, free-space coupling of light into and from WGMRs is very challenging. In previous schemes, resonators are intentionally deformed to break circular symmetry to enable free-space coupling of carefully aligned focused light, which comes with bulky size and alignment issues that hinder the realization of compact WGMR applications. Here, we report a new class of nanocouplers based on cavity enhanced Rayleigh scattering from nano-scatterer(s) on resonator surface, and demonstrate whispering gallery microlaser by free-space optical pumping of an Ytterbium doped silica microtoroid via the scatterers. This new scheme will not only expand the range of applications enabled by WGMRs, but also provide a possible route to integrate them into solar powered green photonics.

REPORT DOCUMENTATION PAGE (SF298) (Continuation Sheet)

Continuation for Block 13

ARO Report Number 58381.16-EL-PCS
Interfacing whispering-gallery microresonators a...

Block 13: Supplementary Note

© 2014 . Published in Scientific Reports, Vol. Ed. 0 4, (0) (2014), (, (0). DoD Components reserve a royalty-free, nonexclusive and irrevocable right to reproduce, publish, or otherwise use the work for Federal purposes, and to authorize others to do so (DODGARS §32.36). The views, opinions and/or findings contained in this report are those of the author(s) and should not be construed as an official Department of the Army position, policy or decision, unless so designated by other documentation.

Approved for public release; distribution is unlimited.



OPEN

SUBJECT AREAS:
MICRORESONATORS
NANOPARTICLES
GREEN PHOTONICS

Received
16 January 2014

Accepted
26 August 2014

Published
17 September 2014

Correspondence and
requests for materials
should be addressed to
L.Y. (yang@seas.wustl.
edu); S.K.O.
(ozdemir@ese.wustl.
edu) or J.Z. (jzhu@
seas.wustl.edu)

Interfacing whispering-gallery microresonators and free space light with cavity enhanced Rayleigh scattering

Jiangang Zhu¹, Şahin K. Özdemir¹, Huzeyfe Yilmaz¹, Bo Peng¹, Mark Dong², Matthew Tomes², Tal Carmon³ & Lan Yang¹

¹Department of Electrical and Systems Engineering, Washington University, St. Louis, MO 63130, USA, ²Department of Electrical and Computer Engineering, University of Michigan, Ann Arbor, MI 48109, USA, ³Department of Mechanical Engineering, Technion, Haifa 3200003, Israel.

Whispering gallery mode resonators (WGMRs) take advantage of strong light confinement and long photon lifetime for applications in sensing, optomechanics, microlasers and quantum optics. However, their rotational symmetry and low radiation loss impede energy exchange between WGMs and the surrounding. As a result, free-space coupling of light into and from WGMRs is very challenging. In previous schemes, resonators are intentionally deformed to break circular symmetry to enable free-space coupling of carefully aligned focused light, which comes with bulky size and alignment issues that hinder the realization of compact WGM applications. Here, we report a new class of nanocouplers based on cavity enhanced Rayleigh scattering from nano-scatterer(s) on resonator surface, and demonstrate whispering gallery microlaser by free-space optical pumping of an Ytterbium doped silica microtoroid via the scatterers. This new scheme will not only expand the range of applications enabled by WGMRs, but also provide a possible route to integrate them into solar powered green photonics.

The last two decades have witnessed a revolution in photonic technologies pioneered on one hand by new concepts in materials and devices such as photonic crystals and metamaterials, and, on the other hand, by the realization and testing of century-old well-known theories such as quantum theory, plasmonics and whispering galleries which have been enjoying many benefits of recent developments in enabling technologies and fabrication techniques^{1–5}. Since its first explanation in acoustic regime by Lord Rayleigh in London's St Paul's Cathedral, WGM phenomenon has been explored in various optical structures for a variety of applications^{6–14}, opening unprecedented and unforeseen directions in optical sciences. Recent advances in fabrication techniques and material sciences have helped to achieve WGMRs with high-quality (Q) factors and nano/micro-scale mode volumes (V). Novel applications and devices using WGMRs have been demonstrated, such as ultra-low threshold on-chip microlasers^{7,8,15,16}, narrowband filters and modulators for optical communication^{9,10,17}, high performance optical sensors achieving label-free detection at single-particle resolution^{1,4,5,11,12}, cavity opto-mechanics^{2,18,19}, quantum electrodynamics^{3,13}, and nonreciprocal optical devices utilizing the concepts of parity-time symmetry²⁰.

Despite their great promises for photonic technologies, coupling light into and from WGMRs is intrinsically hindered by their unique feature of rotational symmetry. The circular geometry is also responsible for the deviation from total internal reflection condition, and introduces radiation losses in particular when the wavelength of the light is comparable to the radius of curvature. Thus, an evanescent field channel exists for extracting light from WGMs, and for coupling light into WGMs using prisms, tapered fibers or waveguides^{21–25}. Coupling efficiency with tapered fibers can reach values as high as 99%. However, achieving this coupling and maintaining it for long durations require active stabilization and precise alignment with nano positioning systems, because coupling conditions are prone to environmental perturbations (e.g., air flow and mechanical vibrations). This significantly limits the practical use of fiber-taper-coupled WGMRs. Prism and on-chip waveguide couplers are more stable, but their applications are limited by the bulkiness of prism system, or the requirement of additional optics to couple light into the on-chip waveguide. Alternative to evanescent coupling techniques is free space coupling (edge coupling) to asymmetric WGMRs such as spiral, ellipsoid, quadrupole and limacon, where circular symmetry is lifted by introducing controlled deformations either after the WGMRs are fabricated or during lithographic patterning^{26–32}. Free-space coupling into and directional emission from deformed/asymmetric resonators are possible due to the dynamic tunneling between the co-existing chaotic and regular WGM modes, which help the light to escape from or couple into the resonator along the direction of deformation. Coupling of free

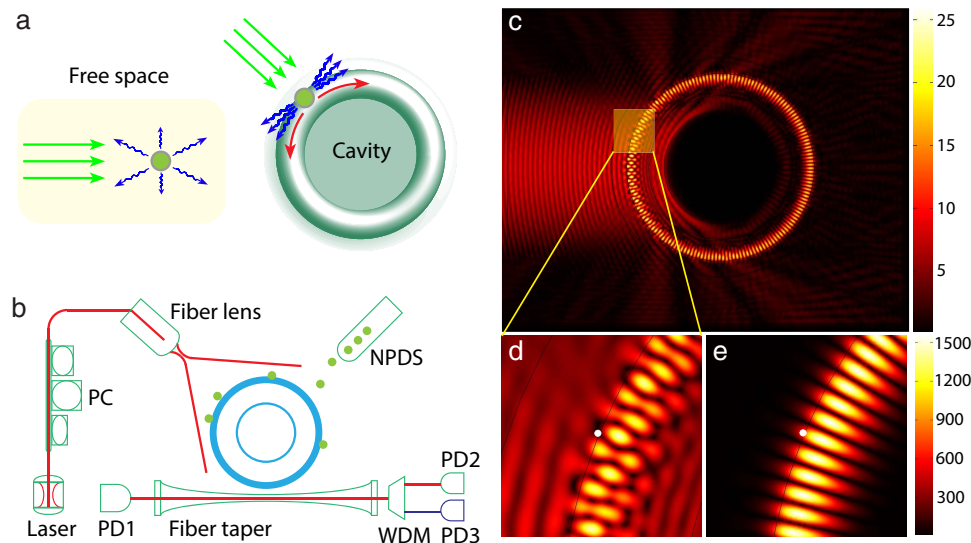


Figure 1 | Coupling of free space light into whispering gallery modes via nano-scatterers. (a), Cavity enhanced light collection. A nanoscale structure usually scatters light in all directions; when a nano-scatterer is placed close to a cavity, most of the scattered light is collected into the cavity mode due to Purcell enhancement. (b), Simplified scheme used for characterizing the performance of the nanocoupler. Light from a tunable laser is sent through a fiber lens and incident onto the resonator. The distance between the fiber lens and cavity is tunable. A fiber taper is used to monitor the light field inside the cavity. PC: polarization controller. WDM: wavelength division multiplexer. NPDS: nanoparticle delivery system. (c), Finite element simulation shows free space light cannot couple into a WGM resonator by direct illumination. (d), Magnified view of the WGM area in (c). (e), With a nanoparticle on the surface of resonator, WGM is efficiently excited from free space. In (d) and (e), the location of nanoparticle was marked with white dot.

space light into such resonators still remains as a challenge, mostly because it relies significantly on precise alignment of the focused free-space light on the cavity edge along the direction of deformation, which requires optical and mechanical systems with high angular and translational resolution. These unavoidably make the system bulky and difficult to move out of the lab environment. Moreover, with the exception of a few studies, such cavities suffer from significant Q-degradation as the degree of deformation is increased. Here we introduce a new interface between the free space light and the WGMs of circular resonators. This interface is formed by directly depositing nano-scatterers or nanoparticles onto the circular WGM. We show that each of the nanoparticle deposited on the resonator surface effectively acts as a nanocoupler to couple free space light into WGMs without additional bulk optical components and precise alignment processes. Further, we demonstrate lasing in an Ytterbium (Yb^{3+}) doped silica microtoroid. Cavity-enhanced Rayleigh scattering lies at the heart of our nano-scale interface between the micro-scale WGM and the free-space light field³³. The hybrid microresonator-nanoparticle system here enables the collection of a large fraction of the scattered light into the cavity mode via Purcell enhancement, and has the ability to harvest even weak light fields. This nanocoupler scheme brings together and relies on four fundamental observations. First, coupling of an emitter to a cavity mode enhances its spontaneous emission rate by increasing the local density of modes, implying that the emitter will emit mostly into the cavity modes and with much faster rate than in vacuum. This enhancement is proportional to Q/V and is known as Purcell enhancement factor. Second, a sub-wavelength particle (i.e., the nanocoupler) can be treated as an oscillating dipole, with the dipole moment induced by the electric field of the incident light, radiating into the surrounding (i.e., Rayleigh scattering). For the resonator, there is no difference between the light coming from an emitter placed in its proximity and the light coming via scattering from a nanoparticle illuminated by a free-space incident light. Thus, Purcell enhancement should take place leading to collection of the weak scattered-light into the cavity WGM. Third, when a nanoparticle is placed close to a resonator and interact with the evanescent field of the resonator, light scattering back into the WGM and also to the

free-space reservoir modes takes place. Here, Purcell effect manifests itself again by enhancing the coupling of the scattered light back into the degenerate WGMs (i.e., over 95% of the scattered light is coupled back^{34,35}). Fourth, nanoscatterers on the resonator break its rotational symmetry thus open a channel for coupling light in and out of WGMs^{36,37}. Therefore, the proposed nanocoupler should provide an efficient route for free-space coupling of light to and from WGMs. An illustration of the concept is given in Fig. 1.

We have developed a theoretical model (Supplementary Note 1) and performed extensive numerical simulations (Supplementary Note 2) to quantify the interaction between free-space light and a WGM with and without perturbing nanoparticles of spherical shape. Figure 1c clearly shows that in the absence of nanoparticles, free-space light does not couple into WGMs while the presence of a single nanoparticle opens up a channel, which interfaces the WGMs inside the resonator with the outside optical modes, including the free-space incident light and the reservoir modes into which the WGMs dissipate.

Results

The setup used in the experiments is depicted in Fig. 1b. It consists of a tunable external cavity laser and a fiber lens as the free-space light source, a fiber-taper coupler to extract the light, which is coupled into the microtoroid from free-space via the nanocouplers, out from the WGM, and a nanoparticle delivery system to deposit the nanoparticles onto the resonator (see Supplementary Fig. 1 and Method 1 for details). The light extracted from the WGM through the fiber-coupler is evaluated using optical spectrum analyzer (OSA) and photodiodes. Fiber-taper coupler enables efficient and tunable out-coupling of the light from the microtoroid for accurate evaluation of the proposed nanocoupler. To evaluate the performance of the nanocoupler, we performed three sets of experiments using this scheme.

In the first set of experiments, we investigated the effect of nanocoupler-resonator and resonator-taper coupling strengths, quantified by 2Γ and κ_1 , respectively (see Supplementary Note 1), on the intracavity power using a free space light whose spot size was larger than the area of the resonator so that all the nanocouplers were

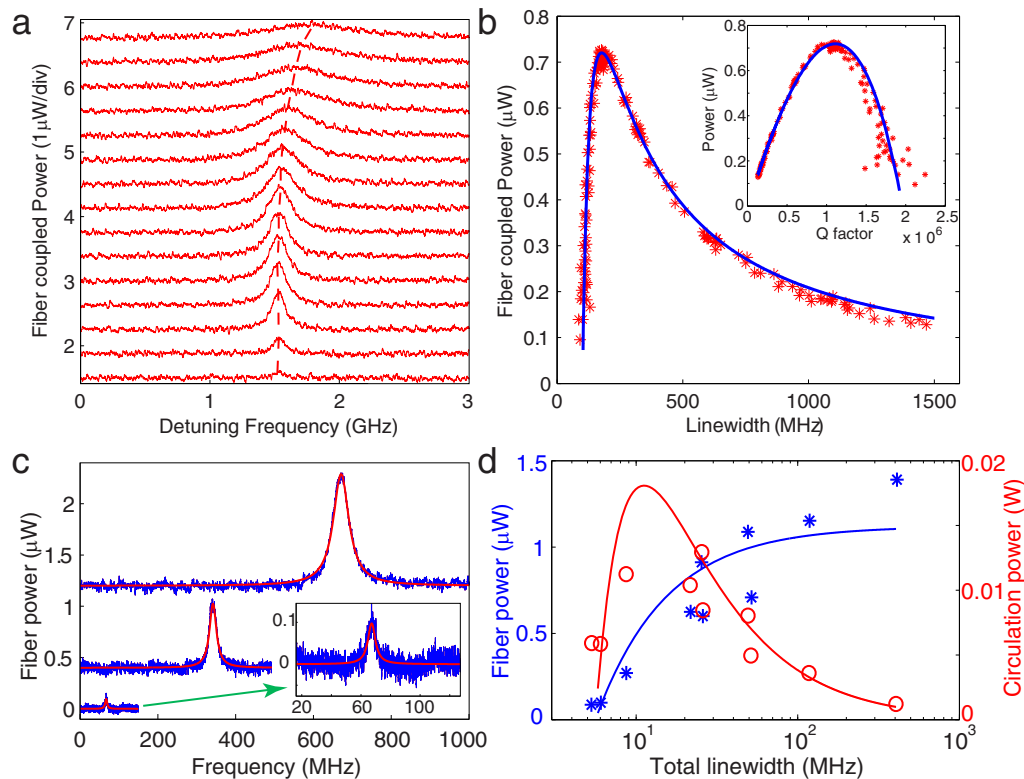


Figure 2 | Loading curves of nanocoupler-resonator-taper system. (a), Spectra of a WGMR, with input light coupled from free space into the resonator via nanocouplers, obtained at different fiber-taper coupling strength quantified by κ_1 . The upper two spectra are vertically shifted up by 0.375 and 0.75 from the lower one for clarity. From bottom to top: the air gap between the fiber taper and the resonator decreases (κ_1 increases). (b), Power coupled out from the WGMR by the fiber taper versus the total linewidth of the nanocoupler-resonator-taper system when κ_1 is increased. Inset shows the power out-coupled using the fiber taper versus total Q factor. The blue fitting curve is obtained using theoretical model described in Supplementary Note 1, and considering a cavity loss factor proportional to κ_1 induced by the non-ideal fiber taper. (c), Mode spectra with increasing number of particles deposited on the microtoroid (increasing 2Γ). Spectra are vertically shifted for clarity. From bottom to top: particle number increases. For each spectrum, fiber taper coupling is optimized to obtain the maximum on-resonance power ($\kappa_1 = \kappa_0 + 2\Gamma$). The inset shows a magnified view of the spectrum with lowest peak power. (d), Blue asterix: power coupled from WGM using the fiber taper versus total linewidth of the system when more particles are deposited. Red circles: Calculated intra-cavity power versus total linewidth. Solid curves are fitting functions obtained from the theoretical model. For these experiments, the input power of free space laser beam is about 2 mW, and wavelength is in 1550 nm band.

illuminated from the top at an angle of about 45-degrees. In this way, we avoided edge coupling and investigated the collective response of all possible coupling channels (nanocouplers). Before depositing any nanoparticles, we tested whether any WGM is excited with this illumination configuration. The result was that no WGM was excited confirming that this configuration of illumination avoids edge-coupling of free-space light into WGMs. Then we monitored the fiber-taper output as the nanoparticles were deposited. We continued nanoparticle deposition until enough power was transmitted from free space into the resonator through the coupling channels made available by the nanoparticles. We specifically chose a large resonator having a large mode volume to prevent or reduce the possibility of observable mode splitting (i.e., amount of mode splitting scales inversely with V). Using a nano positioning system, we changed κ_1 by tuning the taper-resonator distance and monitored the out-coupled light from fiber taper as the wavelength of the free-space light is scanned (Fig. 2a). Since the WGM resonator supports two counter-propagating modes (clockwise, CW and counterclockwise, CCW) at the same resonance frequency, the free space light is coupled into both CW and CCW modes. We observed clear resonance peaks in both the forward (PD1) and the backward (PD2) directions implying the coupling of free-space light into WGM via the nanoparticle based interface (nanocoupler). The extracted light intensity changed as the distance between the resonator and the fiber taper (i.e., air gap) was changed (Fig. 2a,b). As shown in Fig. 2a, in the

deep-under-coupling regime ($\kappa_1 \ll \kappa_0 + 2\Gamma$), the sum of the intrinsic resonator loss κ_0 and the loss induced by the nanocouplers 2Γ dominated the fiber-coupling loss κ_1 ; thus, only a small amount of light was extracted from WGM. Decreasing the air gap brought the system closer to the critical coupling ($\kappa_1 = \kappa_0 + 2\Gamma$), which was accompanied by an increase in the extracted light power at the resonance wavelength; the extracted power reached its maximum value at the critical coupling condition. Further decrease of the air gap moved the system to over-coupling regime (i.e., fiber-coupling loss dominates other losses $\kappa_1 \gg \kappa_0 + 2\Gamma$) and led to reduction in the extracted peak power and to an increase in the linewidth of the resonance peak due to increased loss. We estimated the Q as 10^6 at the critical coupling point, and $\sim 2 \times 10^6$ at the deep-under-coupling regime, which is consistent with the definition of critical coupling condition (Fig. 2b). There is a slight difference between the data obtained in our experiments and the theory based on an ideal coupling model^{22,38}. This difference is the result of the deviation of the fiber-taper coupler from ideality, which introduces additional losses that becomes prominent when the fiber-taper is very close to the resonator. Since the theoretical model assumes an ideal fiber-taper coupler, such losses are not accounted for. This effect is also seen in Fig. 2a, which shows a small resonance shift in the over-coupling regime. In Fig. 2b, the fitting curve is obtained using the model based on the ideal taper-coupler, and by considering an extra cavity loss factor proportional to κ_1 as the free parameter.

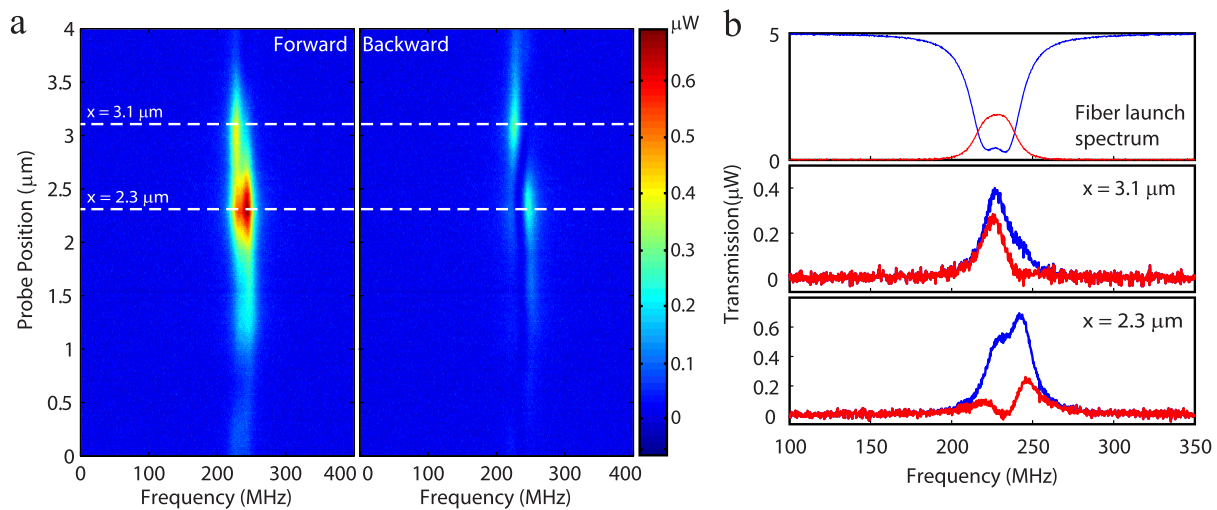


Figure 3 | Mode spectra of a WGMR with incident beam spot at different positions. (a), Spectrograms of light coupled out of the WGMR by a fiber taper in the forward and backward directions when a tightly focused free-space beam spot was scanned along the equator of the microtoroid with nanocouplers. The size of beam spot was about 5 μm . The input power of free space laser beam was about 5 mW, and wavelength is in 1550 nm band. (b), Light coupled out from the microtoroid via a fiber taper when the same fiber taper was used to couple light into the microtoroid (top panel) and when free-space light is coupled into the microtoroid via the nanocouplers within the beam spot size (middle and bottom panels). The transmission spectra in the middle and bottom panels correspond to the probe positions of 3.1 μm and 2.3 μm in (a). Different probe positions yield distinctively different spectra. Blue and red curves denote the transmission spectra in the forward and backward directions, respectively.

Increasing the number of nanoparticles (channels, nanocouplers) increased the number of coupling channels between the WGM and its environment (i.e., increasing 2Γ) and thus led to broader resonance linewidth (i.e., $2\Gamma + \kappa_0 + \kappa_1$) and to more light coupled from free space to WGMs at resonance (Fig. 2c,d). For each measurement depicted in Fig. 2c,d, we fixed the number of nanoparticles and optimized κ_1 such that $\kappa_1 = \kappa_0 + 2\Gamma$ was satisfied. Thus, power extracted from the WGM via the taper was maximized. In this case, the maximum intracavity power was achieved at the critical coupling of nanocoupler-resonator system quantified by $2\Gamma = \kappa_0$ (Fig. 2d). Further increase of the number of nanocouplers (larger 2Γ) shifted the system beyond this critical point and lowered the intracavity power by increased particle-induced dissipation. Because of the random placement of nanoparticles, there is deviation of this specific set of experiments from the theoretical curve. However, averaged results of a large number of simulations follow closely the trend indicated by Eq. S13 and S14 (Supplementary Note 3). These results (Fig. 2) are similar to what has been observed for an add-drop filter configuration where a resonator is coupled to two fiber taper couplers simultaneously³⁹. The experimentally observed dependence of extracted power and the intracavity power on κ_1 , κ_0 and 2Γ agrees well with theoretical model (see Supplementary Note 1).

In the second set of experiments, we started with a resonator-nanocouplers system with observable mode splitting in the transmission spectra (Fig. 3b) and investigated the response of local channels (nanocouplers) by changing the position of a tightly focused free-space beam spot along the equator of a microtoroid. One of the reasons we used a smaller beam spot is to avoid the area where edge coupling is allowed. We can specifically work in the area where nanoparticles are deposited and study nano-scatterer coupling scheme. In this way, we opened only the local channels within the small beam spot size for coupling free space light into WGMs, and recorded the extracted light in both forward (PD1) and backward (PD2) directions as a function of the beam spot position. In such a case when mode splitting exists, the light inside the resonator is expressed as two orthogonal standing wave modes formed by the superposition of the CW and CCW modes^{36,37,40}; the first standing wave mode SWM1 is expressed as $a_{\text{swm1}} = (a_{\text{CW}} + a_{\text{CCW}})/\sqrt{2}$ and the second standing wave mode SWM2 is expressed as

$a_{\text{swm2}} = (a_{\text{CW}} - a_{\text{CCW}})/\sqrt{2}$. The spatial distribution of these modes are $\pi/2$ -phase shifted from each other with the phase describing the spatial distance between the nodes of the SWMs, and the distance between two adjacent nodes of a SWM corresponding to π . As we scanned the beam spot along the resonator surface, we observed distinct spectra at different positions due to the fact that at each position different sets of local nanocouplers were excited and consequently different local channels were opened. Mode splitting was observed in both the forward and the backward transmission spectra. While some sets of local channels coupled light strongly into the SWM1, the other sets of local channels coupled light strongly into the SWM2. This reveals that the nanocouplers channel more free space light into the mode that has stronger spatial overlap with the nanocouplers. If the excited couplers are closer to the node of a mode, either no light or only a small amount of light can be coupled to that mode. These features are clearly seen in Fig. 3b, where split modes show different heights at different probe positions. The discrepancy in the intensity of the two modes is attributed to the different coupling channels and the variation (phase and amplitude) in the light coupled to each of these channels. We also observed that the intensities of the light coupled out in the forward and backward directions were not the same (Fig. 3). This is because the placement of nanoparticles was not symmetric with respect to forward and backward directions, which gave different phase for the forward and backward light. In this case the CW and CCW light inside the resonator were no longer the same.

In the third set of experiments, we demonstrated that the free-space-to-WGM coupling efficiency of the proposed nanocoupler scheme was sufficient to obtain WGM microlasers (Fig. 4). Using free-space light from a tunable laser in the 980 nm band, we observed WGM lasing in the 1050 nm band from an Yb^{3+} -doped silica microtoroid^{41,42}. Lasing started when sufficiently high pump power was built-up in the microcavity (Fig. 4c). The lasing threshold depends on the spatial overlap between the lasing and the pump mode as well as the spectral overlap between WGMs and the absorption and emission bands of Yb^{3+} ions. In the experiments whose results are depicted in Fig. 4c, we used a fiber-taper with thickness optimized to achieve phase matching for the pump mode. The taper-resonator system was then set at under-coupling condition so that only a small

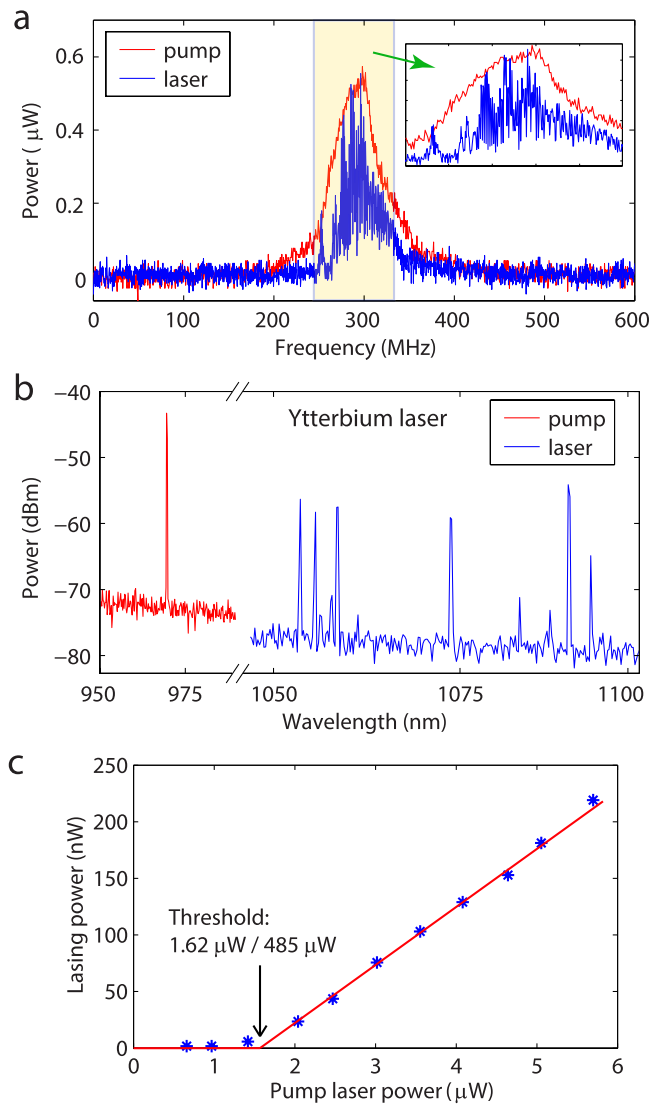


Figure 4 | Whispering gallery mode microlasers by free space excitation via nanocouplers on a microtoroid resonator. (a), Lasing from an Ytterbium doped silica microtoroid achieved by free space excitation. The frequency of the free space pump at 975 nm band was scanned across 600 MHz range around a resonance. The red and blue spectra were obtained by out-coupling the field in the microtoroid using a fiber-taper coupler, and they respectively correspond to the pump in the 975 nm band and the generated ytterbium lasing in the 1050 nm band. The diameter of the fiber taper coupler was optimized for maximal out-coupling of 1050 nm band light from the microtoroid. (b), Pump and lasing spectrum of the Ytterbium laser shown in (a). (c), Relationship between lasing power and pump power of a Ytterbium laser. The threshold pump power for the lasing was measured at two different points, and was found to be 1.62 μW when the power was measured at the output of the fiber taper and 485 μW when it was measured at the input end of the fiber lens. The thickness of the fiber taper coupler was optimized for out-coupling of pump light from the microtoroid, but it was kept at under-coupling regime to reduce extraction of pump power.

amount of intracavity pump power could be coupled out without causing a significant disturbance to the intracavity pump power. This out-coupled light allowed us to estimate the intracavity pump power but since it also reduces the intracavity pump power it leads an effective increase in the lasing threshold power. At the under-coupling condition, the out-coupled power is less than 1/3 of that at the optimal (critical) coupling. In our experiment, the intracavity pump

power (estimated as ~ 37.5 mW at threshold level) is much higher than the total free space pump power (485 μW at threshold) due to the cavity enhancement. As a result the gain provided by direction illumination of Yb^{3+} ions with the free-space light can be ignored, and we can safely conclude that the optical gain is due to resonantly enhanced circulating pump power. We observed not only single mode lasing but also multimode lasing within the emission band of Yb^{3+} ions (Fig. 4b). In multimode lasing, mode competition among many modes in the WGMRs may affect the lasing threshold.

Discussion

To compare the nanoscatterer-based coupling of free space light into the WGM with coupling via focusing the free-space light to the edge of the resonator (i.e., tangential to the circular rim) which we call as edge coupling, we conducted an experiment that involved scanning the free space beam from the center to the equatorial edge of a microsphere. When the beam was aligned at the edge of the microsphere, light was coupled directly into the WGM, as shown by the mode in Fig. 5, at position I. When the beam was moved (in the equatorial plane) away from the edge in the azimuthal direction, edge coupling efficiency decreased rapidly. However, when the beam spot overlapped with scattering centers on the microsphere, we saw the excitation of WGMs again, as shown in Fig. 5, at position II and III, which clearly shows scatterer-based coupling scheme works at different regimes than edge coupling.

In our nanoscatterer-based coupling scheme, it is, in principle, possible to couple light at any incidence angle of the free-space light onto the resonator provided that the dipole moment induced by the free space light is not orthogonal to the electric field of the cavity mode³³. Here we show experimentally-obtained transmission spectra at different illumination configurations where the free space light was focused on the scattering center at different polar (Fig. 6a) and azimuthal angles (Fig. 6b). In theory, both TE and TM modes are sensitive to the changes in the polar angle. At zero-degree polar angle the coupling to TE mode is maximized. TM modes in theory cannot be coupled at zero-degree polar angle, but it can be coupled from 90-degree polar angle. Different polar angles change the alignment between the induced dipole and E field of WGM. In Fig. 6a, despite the presence of mode splitting, it is clear that the WGM excited by the free-space light is a TE mode because free-space light is coupled into this mode efficiently at zero-degree polar angle. Any deviation from the zero-degree polar position decreases the coupling efficiency. The same TE mode is not sensitive to the changes in the azimuthal angle (Fig. 6b), because the induced dipole (in the direction of in/out of the plane) is always aligned with the electrical field of the WGM.

In summary, we have introduced a simple yet elegant and nanocoupler scheme to couple free-space light into WGMRs. The nanocoupler is based on nano-scatterers deposited onto the WGMR. We have observed enhanced light coupling into the WGM through the channels opened by this nanocoupler scheme, and demonstrated WGM lasers using free-space pumping of the resonator via this nanocoupler. With a single nanoparticle, the coupling rate is small (less than 1% of total free space input power) due to the extremely small optical scattering cross-section of a nanoparticle. However, the intracavity power reaches values 100-fold larger than the total input free space power due to resonance enhancement (see Supplementary Note 3). Even with 1% coupling efficiency, the intracavity field intensity is high enough to generate lasing and to perform WGM-based sensing. One could further enhance the coupling efficiency by placing the nanoscatterers in well-defined locations on the resonator with equal distances between them to facilitate constructive interference. The nanoscatterers used to couple light into the cavity can also be used for out-coupling of light. This is possible because the nanoscatterers also open out-coupling channels for the laser generated inside the cavity by scattering it to the surrounding. The scattered laser light then can be detected by photodetectors or an imaging

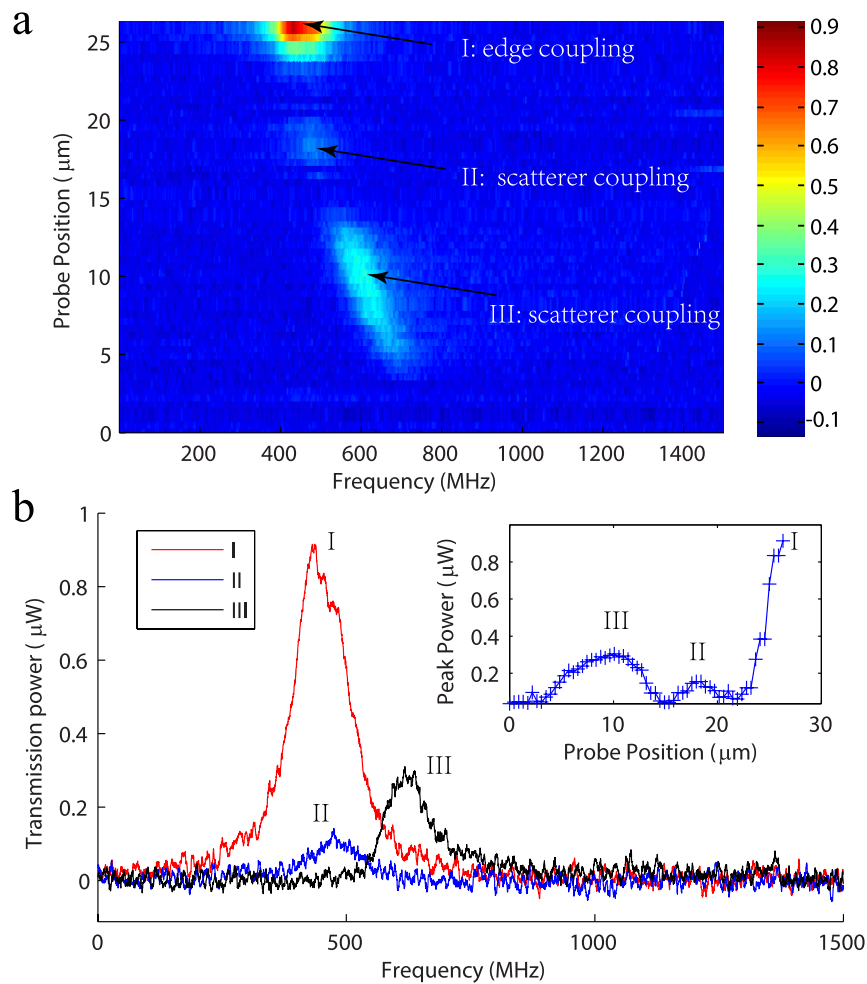


Figure 5 | Coupling of free-space light into a WGM resonator when the free space light beam was moved from the center to the edge of a microcavity. Edge coupling is clearly seen at position I, and nano-scatterer coupling is seen at positions II and III. (a). Spectrogram of fiber taper collected transmission from the cavity. Light is coupled into the sphere from a free space laser beam in 1550 nm band. The shift of the resonance frequency may be attributed to the changes in the phase of input light incident on different scatterers as the probe position changes, and also to thermal drift. (b). Transmission spectra at different probe positions. Inset shows the peak power of the transmission mode at different probe positions.

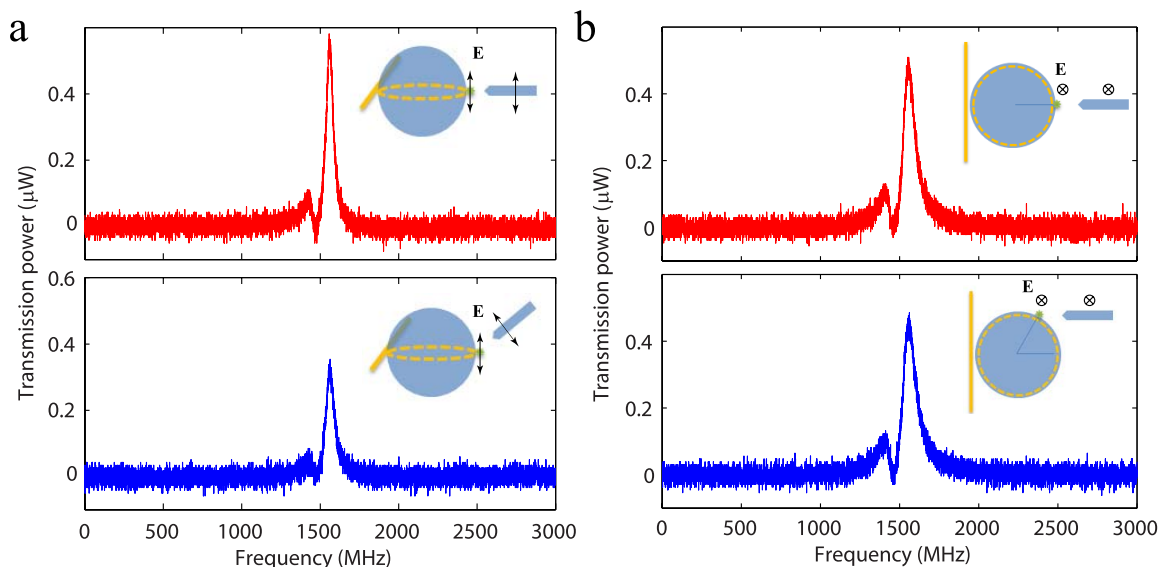


Figure 6 | Angle dependence of free space coupling using nano-scatterers. (a). Free space coupled transmission when the polar angle of the free space beam changed from 0 degrees to 45 degrees. (b). Free space coupled transmission when the azimuthal angle of the free space beam changed from zero to 60 degrees. The directions of electrical field of the WGM and free space light is marked in all figures. It is evident that this mode is a TE mode because in theory light cannot be coupled into TM mode at a polar angle of zero-degree. The green dots in the inset figures are the nano-scatterers.



system placed near the resonator. We believe that this study lays the foundation for future on-chip solar/non-coherent light pumped microlasers, and will greatly facilitate miniaturized WGM resonator applications without complicated coupling optics, and free from chaotic behavior often observed in deformed cavities. Also significant is the inherent local enhancement near the nanoparticles (i.e., optical hot spots due to increased refractive index or plasmon effect) which can dually serve for considerably enhancing sensing¹².

1. Vollmer, F. *et al.* Protein detection by optical shift of a resonant microcavity. *Appl Phys Lett* **80**, 4057–4059 (2002).
2. Kippenberg, T. J., Rokhsari, H., Carmon, T., Scherer, A. & Vahala, K. J. Analysis of radiation-pressure induced mechanical oscillation of an optical microcavity. *Phys Rev Lett* **95**, 033901 (2005).
3. Vernooy, D. W., Furusawa, A., Georgiades, N. P., Ilchenko, V. S. & Kimble, H. J. Cavity QED with high-Q whispering gallery modes. *Phys Rev A* **57**, R2293–R2296 (1998).
4. Zhu, J. *et al.* On-chip single nanoparticle detection and sizing by mode splitting in an ultrahigh-Q microresonator. *Nat Photonics* **4**, 46–49 (2010).
5. He, L., Ozdemir, S. K., Zhu, J., Kim, W. & Yang, L. Detecting single viruses and nanoparticles using whispering gallery microlasers. *Nat Nanotechnol* **6**, 428–432 (2011).
6. Vahala, K. J. Optical microcavities. *Nature* **424**, 839–846 (2003).
7. Polman, A., Min, B., Kalkman, J., Kippenberg, T. J. & Vahala, K. J. Ultralow-threshold erbium-implanted toroidal microlaser on silicon. *Appl Phys Lett* **84**, 1037–1039 (2004).
8. Yang, L., Carmon, T., Min, B., Spillane, S. M. & Vahala, K. J. Erbium-doped and Raman microlasers on a silicon chip fabricated by the sol-gel process. *Appl Phys Lett* **86**, 091114 (2005).
9. Ilchenko, V. S., Savchenkov, A. A., Matsko, A. B. & Maleki, L. Whispering-gallery-mode electro-optic modulator and photonic microwave receiver. *J Opt Soc Am B* **20**, 333–342 (2003).
10. Xu, Q. F., Schmidt, B., Pradhan, S. & Lipson, M. Micrometre-scale silicon electro-optic modulator. *Nature* **435**, 325–327 (2005).
11. White, I. M., Oveys, H. & Fan, X. D. Liquid-core optical ring-resonator sensors. *Opt Lett* **31**, 1319–1321 (2006).
12. Dantham, V. R. *et al.* Label-Free Detection of Single Protein Using a Nanoplasmonic-Photonic Hybrid Microcavity. *Nano Lett* **13**, 3347–3351 (2013).
13. Aoki, T. *et al.* Observation of strong coupling between one atom and a monolithic microresonator. *Nature* **443**, 671–674 (2006).
14. Del'Haye, P. *et al.* Optical frequency comb generation from a monolithic microresonator. *Nature* **450**, 1214–1217 (2007).
15. McCall, S. L., Levi, A. F. J., Slusher, R. E., Pearton, S. J. & Logan, R. A. Whispering-Gallery Mode Microdisk Lasers. *Appl Phys Lett* **60**, 289–291 (1992).
16. Min, B. *et al.* Erbium-implanted high-Q silica toroidal microcavity laser on a silicon chip. *Phys Rev A* **70**, 033803 (2004).
17. Rabiei, P., Steier, W. H., Zhang, C. & Dalton, L. R. Polymer micro-ring filters and modulators. *J Lightwave Technol* **20**, 1968–1975 (2002).
18. Carmon, T., Rokhsari, H., Yang, L., Kippenberg, T. J. & Vahala, K. J. Temporal behavior of radiation-pressure-induced vibrations of an optical microcavity phonon mode. *Physical Review Letters* **94** (2005).
19. Park, Y. S. & Wang, H. L. Radiation pressure driven mechanical oscillation in deformed silica microspheres via free-space evanescent excitation. *Optics Express* **15**, 16471–16477 (2007).
20. Peng, B. *et al.* Parity-time symmetric whispering-gallery microcavities. *Nat Phys* **10**, 394–398 (2014).
21. Knight, J. C., Cheung, G., Jacques, F. & Birks, T. A. Phase-matched excitation of whispering-gallery-mode resonances by a fiber taper. *Opt Lett* **22**, 1129–1131 (1997).
22. Cai, M., Painter, O. & Vahala, K. J. Observation of critical coupling in a fiber taper to a silica-microsphere whispering-gallery mode system. *Phys Rev Lett* **85**, 74–77 (2000).
23. Lin, H. B., Huston, A. L., Justus, B. L. & Campillo, A. J. Some Characteristics of a Droplet Whispering-Gallery-Mode Laser. *Optics Letters* **11**, 614–616 (1986).
24. Little, B. E., Laine, J. P. & Haus, H. A. Analytic theory of coupling from tapered fibers and half-blocks into microsphere resonators. *J Lightwave Technol* **17**, 704–715 (1999).
25. Hosseini, E. S., Yegnanarayanan, S., Atabaki, A. H., Soltani, M. & Adibi, A. High Quality Planar Silicon Nitride Microdisk Resonators for Integrated Photonics in the Visible Wavelength Range. *Optics Express* **17**, 14543–14551 (2009).

26. Liu, C. *et al.* Enhanced energy storage in chaotic optical resonators. *Nat Photonics* **7**, 474–479 (2013).
27. Gmachl, C. *et al.* High-power directional emission from microlasers with chaotic resonators. *Science* **280**, 1556–1564 (1998).
28. Lacey, S. & Wang, H. L. Directional emission from whispering-gallery modes in deformed fused-silica microspheres. *Optics Letters* **26**, 1943–1945 (2001).
29. Levi, A. F. J. *et al.* Directional Light Coupling from Microdisk Lasers. *Appl Phys Lett* **62**, 561–563 (1993).
30. Jiang, X. F. *et al.* Highly Unidirectional Emission and Ultralow-Threshold Lasing from On-Chip Ultrahigh-Q Microcavities. *Adv Mater* **24**, Op260–Op264 (2012).
31. Chern, G. D. *et al.* Unidirectional lasing from InGaN multiple-quantum-well spiral-shaped micropillars. *Appl Phys Lett* **83**, 1710–1712 (2003).
32. Wang, Q. J. *et al.* Whispering-gallery mode resonators for highly unidirectional laser action. *P Natl Acad Sci USA* **107**, 22407–22412 (2010).
33. Motsch, M., Zeppenfeld, M., Pinkse, P. W. H. & Rempe, G. Cavity-enhanced Rayleigh scattering. *New J Phys* **12** (2010).
34. Kippenberg, T. J., Tchebotareva, A. L., Kalkman, J., Polman, A. & Vahala, K. J. Purcell-factor-enhanced scattering from Si nanocrystals in an optical microcavity. *Phys Rev Lett* **103**, 027406 (2009).
35. Ozdemir, S. K., Zhu, J., He, L. & Yang, L. Estimation of Purcell factor from mode-splitting spectra in an optical microcavity. *Phys Rev A* **83**, 033817 (2011).
36. Mazzei, A. *et al.* Controlled coupling of counterpropagating whispering-gallery modes by a single Rayleigh scatterer: a classical problem in a quantum optical light. *Phys Rev Lett* **99**, 173603 (2007).
37. Zhu, J., Ozdemir, S. K., He, L. & Yang, L. Controlled manipulation of mode splitting in an optical microcavity by two Rayleigh scatterers. *Opt Express* **18**, 23535–23543 (2010).
38. Spillane, S. M., Kippenberg, T. J., Painter, O. J. & Vahala, K. J. Ideality in a fiber-taper-coupled microresonator system for application to cavity quantum electrodynamics. *Physical Review Letters* **91** (2003).
39. Monifi, F., Ozdemir, S. K. & Yang, L. Tunable add-drop filter using an active whispering gallery mode microcavity. *Appl. Phys. Lett.* **103**, 181103 (2013).
40. Zhu, J., Ozdemir, S. K., He, L., Chen, D. R. & Yang, L. Single virus and nanoparticle size spectrometry by whispering-gallery-mode microcavities. *Opt Express* **19**, 16195–16206 (2011).
41. Yang, L., Armani, D. K. & Vahala, K. J. Fiber-coupled erbium microlasers on a chip. *Appl Phys Lett* **83**, 825–826 (2003).
42. Ostby, E. P. & Vahala, K. J. Yb-doped glass microcavity laser operation in water. *Opt Lett* **34**, 1153–1155 (2009).

Acknowledgments

This work was supported by Army Research Office grant No. W911NF-12-1-0026.

Author contributions

S.K.O. and L.Y. conceived the idea; J.Z. and S.K.O. designed the experiments; J.Z. performed the experiments with help from S.K.O., H.Y. and B.P. Theoretical background and simulations were provided by J.Z., S.K.O., M.D., M.T. and T.C. All authors discussed the results, and S.K.O. and L.Y. wrote the manuscript with inputs from all authors. L.Y. supervised the project.

Additional information

Supplementary information accompanies this paper at <http://www.nature.com/scientificreports>

Competing financial interests: The authors declare no competing financial interests.

How to cite this article: Zhu, J. *et al.* Interfacing whispering-gallery microresonators and free space light with cavity enhanced Rayleigh scattering. *Sci. Rep.* **4**, 6396; DOI:10.1038/srep06396 (2014).



This work is licensed under a Creative Commons Attribution-NonCommercial-ShareAlike 4.0 International License. The images or other third party material in this article are included in the article's Creative Commons license, unless indicated otherwise in the credit line; if the material is not included under the Creative Commons license, users will need to obtain permission from the license holder in order to reproduce the material. To view a copy of this license, visit <http://creativecommons.org/licenses/by-nc-sa/4.0/>

Supplementary Information -

Nanocouplers for free-space excitation of whispering-gallery microlasers

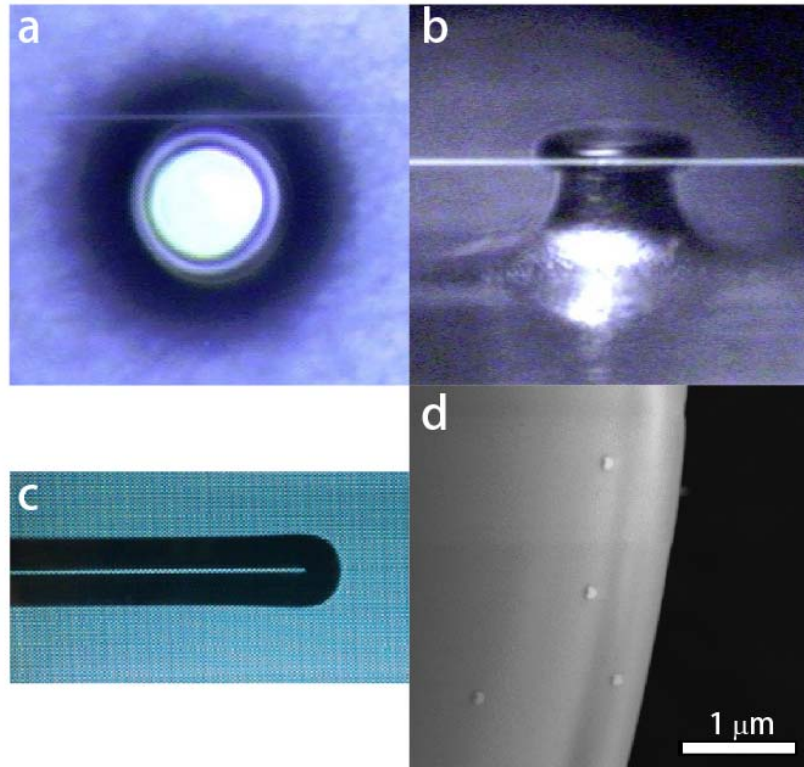
Jiangang Zhu^{1*}, Şahin K. Özdemir^{1*}, Huzeyfe Yilmaz¹, Bo Peng¹, Mark Dong²,
Matthew Tomes², Tal Carmon², and Lan Yang^{1*}

¹Department of Electrical and Systems Engineering, Washington University, St. Louis, MO
63130, USA

²Department of Electrical and Computer Engineering, University of Michigan, Ann Arbor, MI
48109, USA

*Correspondence to: yang@ese.wustl.edu, ozdemir@ese.wustl.edu, jzhu@seas.wustl.edu

Supplementary Figures



Supplementary Figure S1 / Experimental images. *a*, Image of a microtoroid with diameter of about 80 μm coupled with a tapered fiber, top view. *b*, side view of *a*. *c*, Optical image of the fiber lens made from a single mode fiber (SMF-28e). *d*, Polystyrene nanoparticles (radii 50 nm) deposited on the surface of a microtoroid.

Supplementary Method 1

Fabrication and Experiment setup

To study the free space light coupling using nanocouplers, we fabricated passive microtoroids with major diameters of 60-150 μm using commercially available silicon wafers with 2 μm oxide layer. We also fabricated active microtoroids using sol-gel method¹⁶, either using an Ytterbium-doped (Yb^{3+} concentration: $2 \times 10^{18}/\text{cm}^3$ to $2 \times 10^{19}/\text{cm}^3$) sol-gel silica layer (3 layer coating, 1.5 μm total thickness) on silicon or by coating a silica (no dopant) microtoroid resonator with Yb^{3+} -doped sol-gel followed by CO_2 laser annealing. The details of fabrication process can be found in Ref. 16 of the main text. Fabricated microtoroids had optical Q factors in the range of 5×10^6 - 10^8 . We have also fabricated passive microspheres by melting the end of tapered fibers using fusion splicer (Ericsson FSU 995FA) or CO_2 laser pulses. Active microspheres were made by dip-coating passive ones into the sol-gel solution containing Yb^{3+} (ion concentration $2 \times 10^{18}/\text{cm}^3$ to $2 \times 10^{19}/\text{cm}^3$) followed by high temperature annealing. The resulting passive and active microspheres had Q factors between 10^7 and 10^8 .

Tapered fibers^{21,22} used to extract light from microresonators were fabricated by pulling single mode fibers on a hydrogen flame. In order to couple the pump light (free space light coupled into the resonator via the proposed nanocouplers) and the generated laser light (from the rare-earth ions doped into the silica resonators) out from the WGMs of the resonators, we fabricated fiber tapers of varying sizes and selected the ones which achieved optimal or close-to-optimal coupling efficiency. It is worth noting that, due to the wavelength difference between the pump and lasing modes, optimal coupling for the pump (lasing) mode doesn't ensure optimal condition for the lasing (pump) mode. To send laser light from free space to the microresonator, we fabricated a lensed fiber by cleaving a single mode fiber followed by partially reflowing the end using a fusion splicer (Ericsson FSU 995FA). The resulting lensed-fibers (**Fig. S1c**) had focusing distances in the range of 20-100 μm and beam spot diameters of 5-10 μm in 1550 nm wavelength band.

Nanoparticles of known sizes and materials were delivered onto the surface of a resonator by using a system similar to that described in Ref. 4 and 5 in the main text. We used polystyrene nanospheres with radii of 20-75 nm (Thermo Scientific 3000 Series Nanosphere™ Size

Standards) as nanocouplers in our experiments. Nanospheres were dispersed in water and sent through the aerosol particle classification system and finally carried out by ultra-high purity nitrogen and blown onto the resonator using a glass nozzle with end diameter of about 100 μm . The nozzle allows targeting of any microtoroid chosen for deposition. The distribution of particles on the resonator is governed by the nozzle angle and position. Deposited nanoparticles were verified using SEM (**Fig. S1d**).

We probed the WGMs of the resonators using tunable diode lasers (New focus Velocity, TLB-6300-LN controller) in 1550 nm or 980 nm bands. The tunable laser was tuned to match with the resonance modes and then its wavelength was modulated with a triangle wave signal to perform fine-scanning of 0.08 nm around the resonance. The out-coupled light from the fiber taper was monitored with photodetectors (New Focus 1811-FC Photoreceiver, 900-1700 nm, 125 MHz) and data was acquired to a computer through an oscilloscope.

The fiber lens was mounted on a 3D translational stage and pointed at the microtoroid at an angle of about 15 degrees with respect to the plane of the silicon chip. We adjusted the distance between the lens and the resonators using a 3D translational stage to allow maximal coverage of the microtoroid, or, a minimal beam spot on the microtoroid.

Supplementary Note 1

Free space coupling through a single nanoparticle

For a WGM cavity with quality factor Q and effective circumference L , we have:

$$\frac{P_{cav}}{P_{fs}^{\Omega_{cav}}} = \frac{2Q\lambda}{\pi nL} \quad (S1)$$

where $P_{fs}^{\Omega_{cav}}$ denotes the power scattered into the cavity mode in both the clockwise (CW) and the counter-clockwise (CCW) directions under free-space condition (when cavity is not present) and P_{cav} represents the power scattered into the cavity mode, when the cavity is present, which should be equal to the power dissipated by the cavity. Due to *Purcell* enhancement³³⁻³⁵, and taking into account the normalized field distribution $f(\vec{r})$ at the particle location \vec{r} , we find

$$\frac{P_{cav}}{P_{dip} \cdot f^2(\vec{r})} = P = \frac{3Q\lambda_n^3}{4\pi^2 V} \quad (S2)$$

where P_{dip} designates total power scattered into the dipole mode in free space, λ_n denotes the effective wavelength of the WGM mode and V is the mode volume defined as:

$$V = \frac{\int \varepsilon(\vec{r}) |E(\vec{r})|^2 dV}{\max(\varepsilon(\vec{r}) |E(\vec{r})|^2)} \quad (S3)$$

Thus, we have:

$$\frac{P_{fs}^{\Omega_{cav}}}{P_{dip}} = \frac{P_{fs}^{\Omega_{cav}}}{P_{cav}} \frac{P_{cav}}{P_{dip}} = \frac{\pi nL}{2Q\lambda} \frac{3Q\lambda_n^3}{4\pi^2 V} f^2(\vec{r}) = \frac{3L\lambda_n^2}{8\pi V} f^2(\vec{r}) \quad (S4)$$

Since P_{dip} can be evaluated by multiplying the input intensity I_{in} (or E_{in}^2) and the particle cross-section σ_s , we can calculate $P_{fs}^{\Omega_{cav}}$ using:

$$P_{fs}^{\Omega_{cav}} = \frac{3L\lambda_n^2}{8\pi V} f^2(\vec{r}) \cdot I_{in} \sigma_s \quad (S5)$$

This relation can also be obtained by evaluating the overlap integral between dipole radiation mode and a Hermite-Gaussian cavity mode in a mirror cavity³³. Next, we can write the cavity rate equations with one particle of radius r :

$$\begin{aligned}\frac{dE_{CW}}{dt} &= -(i(\Delta\omega + g) + \frac{\kappa_0 + \kappa_1 + \Gamma}{2})E_{CW} - (ig + \frac{\Gamma}{2})E_{CCW} - \frac{i}{\tau_0} \sqrt{\frac{3L\lambda_n^2}{16\pi V}} f^2(\vec{r}) \cdot I_{in} \sigma_s \\ \frac{dE_{CCW}}{dt} &= -(i(\Delta\omega + g) + \frac{\kappa_0 + \kappa_1 + \Gamma}{2})E_{CCW} - (ig + \frac{\Gamma}{2})E_{CW} - \frac{i}{\tau_0} \sqrt{\frac{3L\lambda_n^2}{16\pi V}} f^2(\vec{r}) \cdot I_{in} \sigma_s \\ a_{fiber} &= iE_{CW} \sqrt{\tau_0 \kappa_1}\end{aligned}\tag{S6}$$

where $\Gamma = \frac{\alpha^2 f^2(\vec{r}) \omega_c^4}{6\pi v^3 V}$, $g = -\frac{\alpha f^2(\vec{r}) \omega_c}{2V}$, and $\alpha = 4\pi r^3(n_p^2 - 1)/(n_p^2 + 2)$. Define $E_{sym} = (E_{CW} + E_{CCW})/\sqrt{2}$ as the symmetric eigenmode (the asymmetric eigenmode doesn't receive any input power because the particle is situated at its node). From the above differential equations, we find the rate equation for the symmetric mode as:

$$\frac{dE_{sym}}{dt} = -(i(\Delta\omega + 2g) + \frac{\kappa_0 + \kappa_1 + 2\Gamma}{2})E_{sym} - \frac{i}{\tau_0} \sqrt{\frac{3L\lambda_n^2}{8\pi V}} f^2(r) \cdot I_{in} \sigma_s\tag{S7}$$

At resonance condition $\Delta\omega + 2g = 0$, we find the steady state solution of E_{sym} as

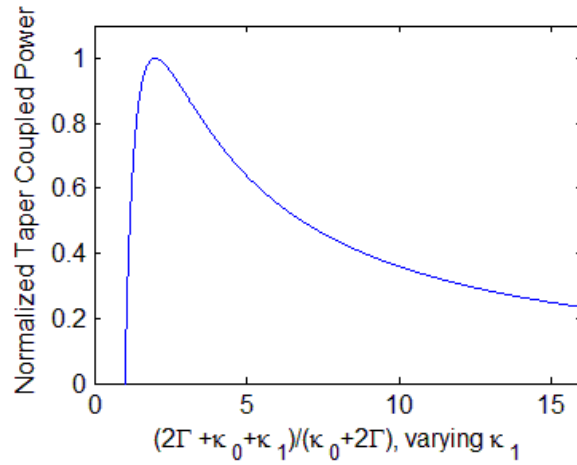
$$|E_{sym}| = \frac{\sqrt{\frac{3L\lambda_n^2}{2\pi V \tau_0^2}} f^2(r) \cdot I_{in} \sigma_s}{\kappa_0 + \kappa_1 + 2\Gamma} = \frac{\sqrt{\frac{3L\lambda_n^2}{2\pi V \tau_0^2}} f^2(r) \cdot I_{in} \frac{8\pi^3 \alpha^2}{3\lambda_n^2}}{\kappa_0 + \kappa_1 + \frac{\alpha^2 f^2(r) \omega_c^4}{3\pi v^3 V}} = \frac{\sqrt{\frac{3\lambda_n^2}{4\pi \tau_0}} \cdot I_{in}}{(\frac{\kappa_0 + \kappa_1}{\sqrt{2\Gamma}} + \sqrt{2\Gamma})}\tag{S8}$$

Here we used $\sigma_s = 8\pi^3 \alpha^2 / 3\lambda_n^4$ and $\Gamma = \alpha^2 f^2(\vec{r}) \omega_c^4 / (6\pi v^3 V)$. If α or Γ is the only variable, when $2\Gamma = \kappa_0 + \kappa_1$, the intensity of the symmetric mode $|E_{sym}|^2$ is maximized (Cauchy-Schwarz inequality). This means that for a single scatterer when the particle induced loss equals to the sum of the all other cavity losses, the intra-cavity power is maximized. Calculations in **Fig. S10** and experiment results in **Fig. 2** of main text verify this conclusion. It is worth noting that this conclusion is also correct for multiple particle case, as suggested in **Fig. 2** of the main text and Fig. S11.

On the other hand, for the fiber taper output, we have:

$$|a_{fiber}|^2 = |iE_{CW}\sqrt{\tau_0\kappa_1}|^2 = |iE_{sym}\sqrt{\tau_0\kappa_1/2}|^2 = \frac{3\lambda_n^2}{8\pi} \cdot I_{in} \frac{2\Gamma\kappa_1}{(\kappa_0 + \kappa_1 + 2\Gamma)^2} \quad (S9)$$

If fiber taper coupling κ_1 is the only variable parameter, then we find that setting it as $\kappa_1 = \kappa_0 + 2\Gamma$ (critical coupling condition) maximizes the fiber output (**Fig. S2**). This conclusion is consistent with the experimental results given in **Fig. 2** of the main text.



Supplementary Figure S2 / Fiber taper coupled power $|a_{fiber}|^2$ versus normalized cavity loss (normalized to $\kappa_0 + 2\Gamma$) with varying κ_1 .

Free space coupling through multiple nanoparticles

When there are multiple scattering centers on the resonator, the scattering light from each scatterer needs to be taken into consideration. Assuming there are N particles, and the light field incident on particle n is $E_{in}^n e^{i\varphi_n}$, the rate equations can be expressed as:

$$\begin{aligned} \frac{dE_{CW}}{dt} &= -(i(\Delta\omega + g_{sym} + g_{asym}) + \frac{\kappa_0 + \kappa_1 + \Gamma_{sym} + \Gamma_{asym}}{2})E_{CW} - (i(g_{sym} - g_{asym}) + \frac{\Gamma_{sym} - \Gamma_{asym}}{2})E_{CCW} - i\sum_{n=1}^N E_{CWin}^n \\ \frac{dE_{CCW}}{dt} &= -(i(\Delta\omega + g_{sym} + g_{asym}) + \frac{\kappa_0 + \kappa_1 + \Gamma_{sym} + \Gamma_{asym}}{2})E_{CCW} - (i(g_{sym} - g_{asym}) + \frac{\Gamma_{sym} - \Gamma_{asym}}{2})E_{CW} - i\sum_{n=1}^N E_{CCWin}^n \end{aligned} \quad (S10)$$

where $E_{CWin}^n = \sqrt{\frac{3L\lambda_n^2}{16\pi\tau_0^2V} f_n^2(\vec{r}) \cdot \sigma_s^n E_{in}^n e^{i(\varphi_n + \beta_n - \phi_N)}} , E_{CCWin}^n = \sqrt{\frac{3L\lambda_n^2}{16\pi\tau_0^2V} f_n^2(\vec{r}) \cdot \sigma_s^n E_{in}^n e^{i(\varphi_n - \beta_n + \phi_N)}} ,$

$\beta_n \in [0, 2\pi)$ is the spatial phase position of the n -th particle^{36,37} assuming that the distance between the nodes of standing wave mode (SWM) corresponds to π , $\varphi_n \in [0, 2\pi)$ is the phase of light incident on the n -th particle and $\phi_n \in [0, 2\pi)$ is the phase position of the anti-node of the symmetric SWM^{36,37}. The scattering and damping terms are defined as^{36,37}:

$$\begin{aligned} g_{\text{sym}} &= \sum_{n=1}^N g_n \cos^2(\phi_N - \beta_n), g_{\text{asym}} = \sum_{n=1}^N g_n \sin^2(\phi_N - \beta_n) \\ \Gamma_{\text{sym}} &= \sum_{n=1}^N \Gamma_n \cos^2(\phi_N - \beta_n), \Gamma_{\text{asym}} = \sum_{n=1}^N \Gamma_n \sin^2(\phi_N - \beta_n) \end{aligned} \quad (\text{S11})$$

where g_n and Γ_n are the scattering and damping coefficients of n th particle. The phase position of standing wave modes can be calculated by³⁷:

$$\tan(2\phi_N) = \frac{\sum_{n=1}^N g_n \sin(2\beta_n)}{\sum_{n=1}^N g_n \cos(2\beta_n)} \quad (\text{S12})$$

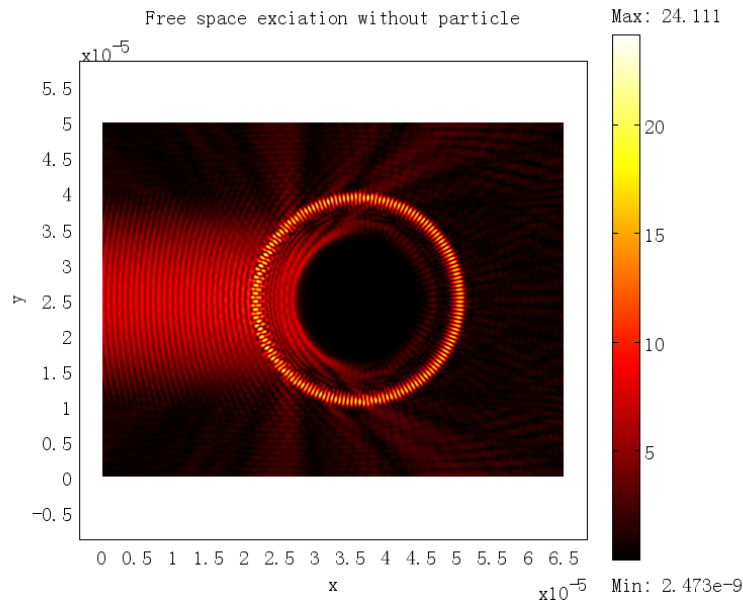
Supplementary Note 2

Finite-element Simulations

To verify our theoretical model and experimental results, we performed finite-element simulations using Comsol Multiphysics. A 2D model is presented to demonstrate the fundamental principles of the nanocoupler scheme. We also calculated the coupling of light into a microtoroid via a nanosphere by using a full 3D model⁴³.

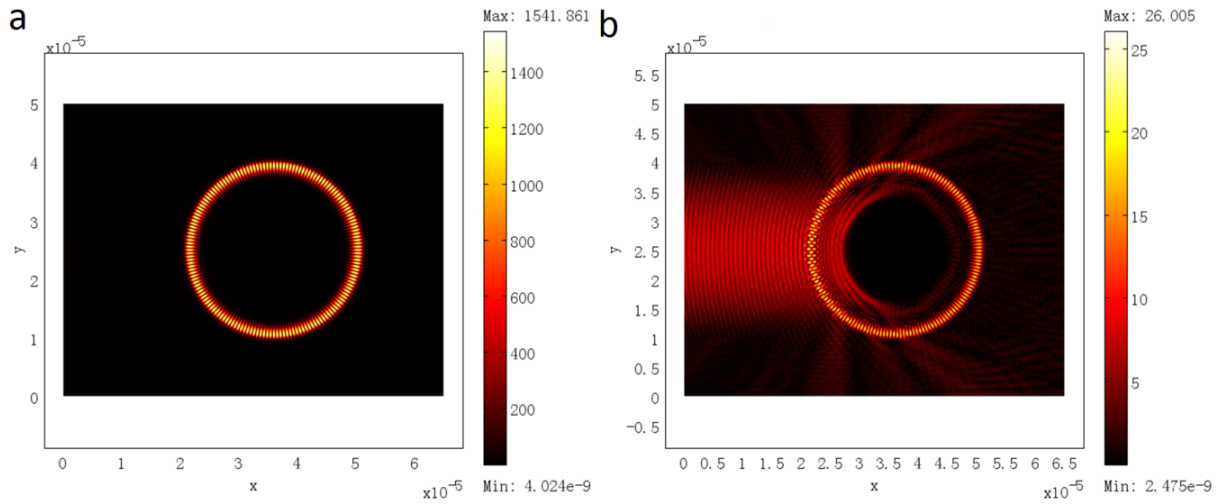
Free space excitation with and without a single nanoparticle

We performed the simulation with a 2D WGM resonator with diameter $30\text{ }\mu\text{m}$ and refractive index $1.45-0.00000001i$, surrounded by air (refractive index of 1). The small imaginary part in the refractive index is introduced to account for the absorption and scattering losses experienced in the experiments. The Q factor of this resonator is 7.375×10^7 . The center of the resonator (outside WGM area) is set to have strong absorption (refractive index of $1-0.5i$) to minimize the lensing effect by the curvature of resonator-air interface. A free space light port with $30\text{ }\mu\text{m}$ width is placed to the left of the resonator.



Supplementary Figure S3 | *Simulated electrical field distribution when free space light is illuminated on a bare resonator (without nanoparticles). WGM is not efficiently excited.*

First, we performed eigenmode analysis to find the resonance frequency and Q factor of the system. Next, we set the frequency of the free space light equal to the resonance frequency of the resonator and conducted harmonic stationary analysis. **Figure S3** shows the simulation result. We calculated the average electrical field strength in the resonator to be 1.219 (a.u.). Although WGM pattern exists in the resonator, the electrical field strength inside the resonator is comparable to that of the input light in free space. In other words, WGM is not efficiently excited. By efficient excitation we mean that there is a significant discrepancy between the electric field strengths in the resonator and in the surrounding, i.e., the former being much larger than the latter due to resonance-enhancement of the field inside the resonator.

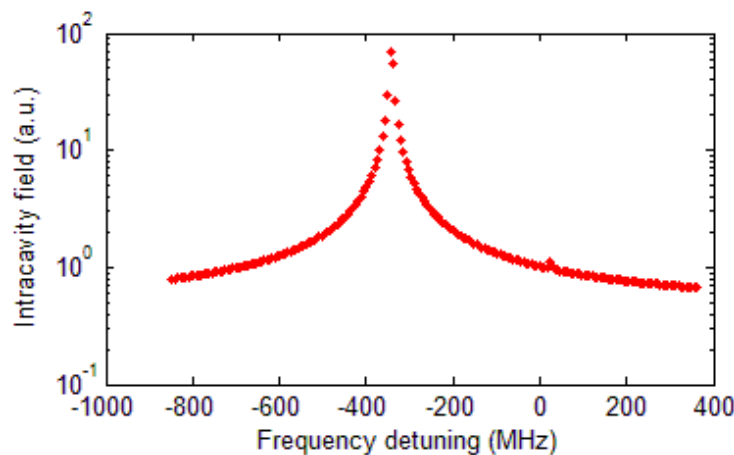


Supplementary Figure S4 | Simulated electrical field distribution when free space light is illuminated on a resonator with a single nanoparticle. a, Symmetric mode, which has maximal overlap with the nanoparticle, is efficiently excited. **b**, Asymmetric mode, which has minimal overlap with the nanoparticle, is not efficiently excited.

Finally, we added a nanoparticle onto the resonator surface and repeated the simulation. The nanoparticle had a radius of 20 nm and refractive index of 1.3. As expected the eigenfrequency of the resonator-particle system showed mode splitting. The Q factor of the symmetric mode (mode whose antinode overlapped with the nanoparticle) decreased to 2.942×10^7 whereas the Q factor of the asymmetric mode (mode whose node overlapped with the nanoparticle) was unchanged (7.375×10^7) compared to the case without the nanoparticle coupler. Then, we performed harmonic stationary analysis with the frequency of the free space light set to the

frequencies of each of the split modes. **Figure S4** shows the simulation results. For the symmetric mode, the light scattered from nanoparticle is efficiently collected into the mode due to optimal overlap between the mode and the particle, and the WGM is efficiently excited. On the other hand, the asymmetric mode receives very little scattered light due to minimal overlap between the mode and the nanoparticle. The average field strength in the resonator was calculated to be 85.75 and 1.286 for the symmetric and asymmetric mode, respectively. According to these numbers, a single nanoparticle increases the intra-cavity power by a factor of about 5000.

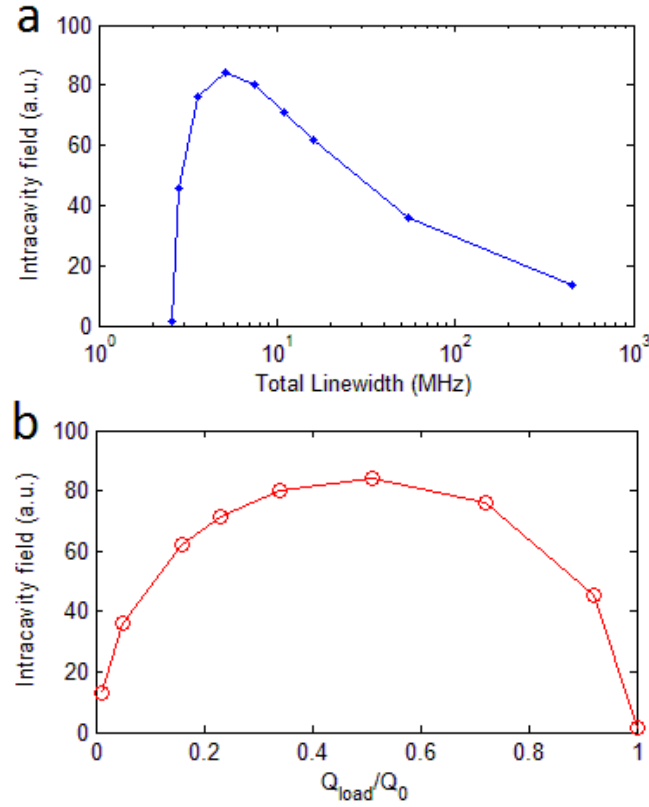
To obtain the frequency response of the resonator-particle system, we performed parametric analysis where the frequency of the free-space light was scanned and the average field strength in the resonator was calculated. **Figure S5** shows the relation between the intra-cavity field and the frequency of the free-space light. The dominant resonance peak at the frequency of symmetric mode implies the efficiency of the proposed nanocoupler scheme to couple free-space light into the cavity and the resonance-enhancement of the intra-cavity field.



Supplementary Figure S5 | *Simulated intra-cavity field strength versus the frequency of the free-space light. A dominant resonance peak at the frequency of symmetric mode and a weak resonance peak at the frequency of asymmetric mode are clearly visible.*

In order to study the effect of nanoparticle polarizability on the intracavity field, we varied the refractive index of the particle from 1 to 3, and keep the particle size unchanged to use the same mesh in the simulations. To compare with experimental results, we obtained the linewidth and Q factor of the symmetric mode when nanoparticle refractive index was increased. **Figure S6**

shows the relation between the intracavity power and the total linewidth or total Q factor. Simulation shows that when the particle-induced loss equals to the sum of all other cavity losses, the intra-cavity field is maximized, which agrees well with theory and our experimental results shown in the main text (**Fig. 2**).



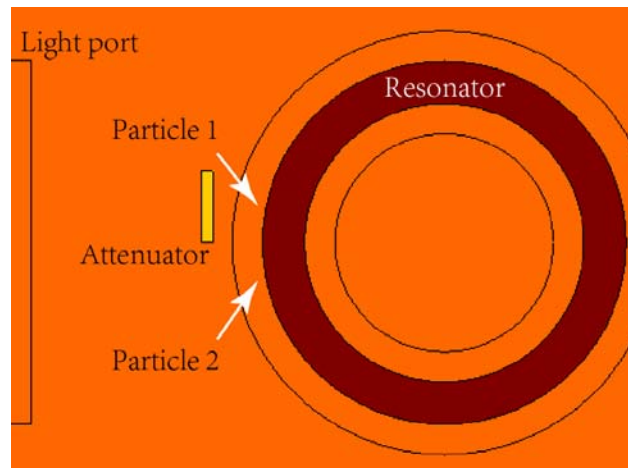
Supplementary Figure S6 | Simulated intra-cavity field strength when nanoparticle induced loss is increased. a, Intra-cavity field versus total linewidth. b, Intra-cavity field versus total Q factor (normalized by Q_0). The intra-cavity field strength reaches maximum when particle induced loss equals cavity intrinsic loss, or $Q_{load} = 0.5Q_0$.

Free space excitation with two nanoparticles

When there are multiple nanoparticles on the resonator, the eigenmodes (standing wave modes, SWMs) inside the resonator no longer locate their node or antinode at the position of nanoparticles. The distributions of SWMs (split modes) are determined by the particle ensembles according to their relative spatial phase positions in the azimuthal direction on the resonator and

their overlap $f(\vec{r})$ with WGM³⁶. As discussed in Sec.2, intracavity power depends not only on the positions of the particles and their overlap with WGM, but also on the intensity and phase of the free-space incident light on each particle.

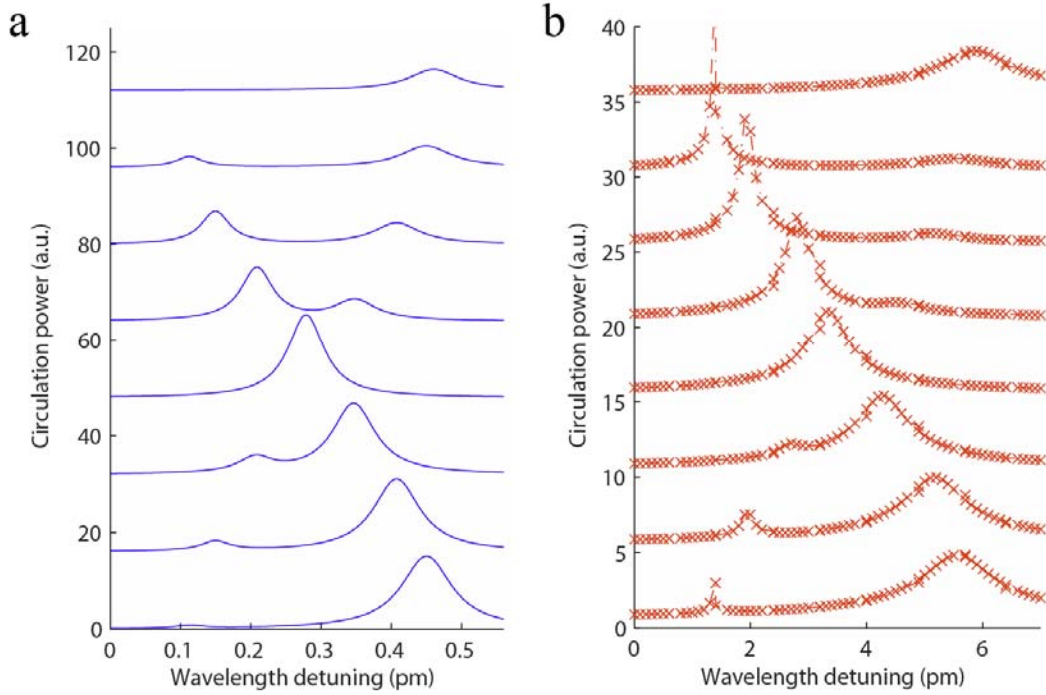
To study this phenomenon, we performed simulations on the simplest case of two particles on the resonator. Similar to the simulation model in the single particle case, we added another particle of the same size on the resonator; the two particles are arranged symmetrically (vertically mirrored) with respect to the axis of the resonator along the direction of the incident light (**Fig. S7**). The phase of the incident light on these two particles was kept the same, and the particles had the same distance to the resonator surface (same overlap $f(\vec{r})$ with WGM). The intensity of light incident on the first particle was decreased to about half of that on the second particle by attenuating the incident light. Note that if the intensity of light incident on two particles is the same, only the symmetric mode can be excited because the system becomes symmetric around horizontal center line. The nanoparticles had radii of 20 nm and refractive index of 1.5-0.05i. The purpose of having a complex refractive index for the nanoparticles is to increase the particle induced loss to compensate the difference in particle scattering properties between 2D and 3D cases. In 2D simulation, nanoparticles scale differently from 3D case, and with the same diameter and refractive index usually give larger mode splitting but smaller particle- induced linewidth broadening compared to the 3D simulation.



Supplementary Figure S7 |Finite-element simulation model with two particles on a resonator.

Two nanoparticles (too small to be seen in the figure) are positioned symmetrically with respect to the horizontal axis of the resonator and light port. An attenuator with refractive index of 1-

0.1i is placed in front of particle 1 to decrease the light intensity incident on the particle. The resonator has diameter of 30 μm and refractive index of $1.45-0.00000001i$ and the nanoparticles have radii of 20 nm and refractive index of $1.5-0.05i$.



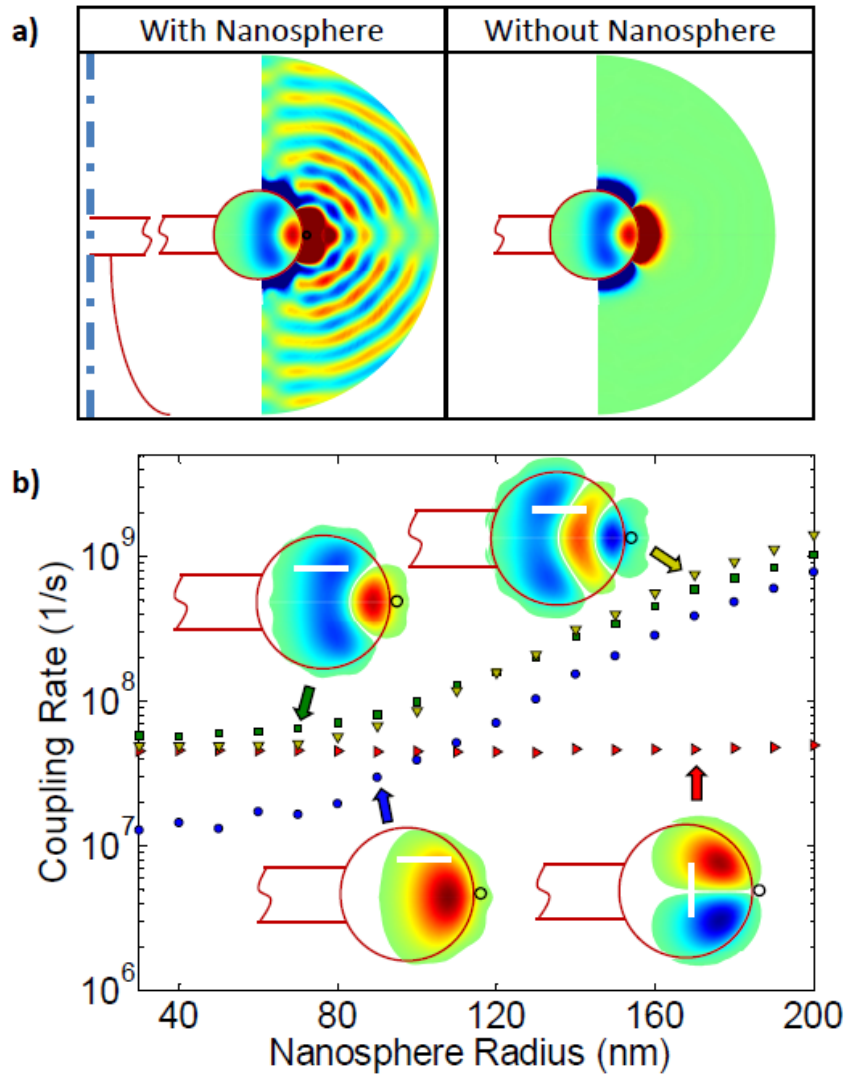
Supplementary Figure S8 |Intracavity power with two nanoparticles on a resonator. The spectra are vertically shifted for clarity. From bottom to top: phase distance between the two particles is increased from $\pi/8$ to π with $\pi/8$ interval. a, Optical spectra of intra-cavity power calculated using the theoretical model. The nanoparticles have radii of 100 nm and refractive index of 1.59. Intrinsic Q factor of the resonator is 7×10^7 . b, Optical spectra of intra-cavity power calculated using 2D finite-element simulations.

We then varied the relative spatial phase distance between the two particles from $\pi/8$ to π at intervals of $\pi/8$, and calculated the relation between average intensity inside the resonator and wavelength using harmonic parametric simulation. **Figure S8** shows the simulation results and compares them with theoretical calculations. Both theoretical and simulation results show mode crossing pattern which is due to the changes in the relative position of nanoparticles³¹. The

simulation results for eigenmode position and field strength agree well with the calculated results from the theoretical model presented in Section 2. Note that since the theoretical model considers a 3D model, there is a slight difference with the numerical simulations based on a 2D model: As seen in **Fig. S8**, the Q of the mode with shorter wavelength is higher in the simulation (**Fig. S8b**) than in the analytical model (**Fig. S8a**) and thus has a higher intracavity power. This can be attributed to the difference in the particle-induced scattering loss in 2D and 3D models. This difference leads to higher Q factor in 2D simulations as the optical mode experiences less loss when the corresponding standing wave mode does not strongly overlap with the particles (**Fig S8b**). Consequently, a higher intracavity circulating power is predicted. Nonetheless, the simulations provide a verification of our theoretical model.

3D model of a microtoroid-nanoparticle system

We also calculated the coupling of light into a microtoroid via a nanoparticle using a fully 3D model⁴³. The toroid is represented by a slice spanning 1.5 wavelengths along the circumference. As expected, with no nanosphere (**Figure S9a**, right) the field is minimally coupled to the surrounding⁴⁴. On the contrary, when a nanosphere is attached to the toroid (**Figure S9a**, left) we see a quasi-spherical wavefront spreading around the nanosphere. In previous studies^{28-29,45} this spherical wave represents light that is scattered out of the toroid by the nanoparticle. Here, on the contrary, this spherical wave represents light that is coming from the surrounding and coupled into the toroid. Both of the above interpretations are valid since this optical system is reciprocal⁴⁶. Though the incoming field in our experiment is not identical with the one calculated, it was sufficiently similar to explain coupling of light into the toroid. Using the same numerical calculation⁴³, we check the coupling rate as a function of the nanoparticle size for various modes. This calculation shows a large difference between the coupling rates for various modes and allows, in principle, a critical coupling condition for the pump mode, while being under coupled for the laser mode in accordance with what is needed for low-threshold lasers.



Supplementary Figure S9 / Simulation results from a 3D model for light coupling from free space to WGMs by a nanoparticle. *a*, The form of the electric field exhibits a quasi-spherical wave with origin at the nanoparticle. A test case with no nanoparticle present is also shown for comparison. *b*, Parametric study of the coupling rate as a function of the nanoparticle size. The toroid major and minor diameters are 50 and 5 μm . The microtoroid and the nanosphere are made of silica ($n = 1.45$) and polystyrene ($n = 1.555$) and the vacuum optical wavelength is near 1.55 μm . In *a*, the electric field outside the resonator has been scaled up by a factor of 100 to be visible, the nanoparticle radius is 200 nm and the optical polarization is horizontal. In *b*, the white lines represent polarization direction.

Supplementary Note 3

Coupling efficiency and Q degradation with a single scatterer

With a single scatterer on the resonator, from Eq. (S8) we have

$$|E_{cw}| = |E_{ccw}| = \sqrt{\frac{3\lambda_n^2}{8\pi\tau_0} \cdot I_{in}} / \left(\frac{\kappa_0 + \kappa_1}{\sqrt{2\Gamma}} + \sqrt{2\Gamma} \right) \quad (\text{S13})$$

To obtain the maximum intracavity power, we need to set $\kappa_1 = 0$ and $2\Gamma = \kappa_0$, implying that there is no fiber taper coupling to extract power from the cavity, and that the scatterer-induced loss is equal to intrinsic cavity loss (i.e., critical coupling). Under this condition, we have $|E_{cw}|_{\max}^2 = |E_{ccw}|_{\max}^2 = 3\lambda_n^2 I_{in} / (32\pi\tau_0\kappa_0)$, where τ_0 is the cavity roundtrip time, and λ_n is the effective wavelength of the cavity mode. We see that the maximum intracavity power is proportional to $1/\kappa_0$ (i.e., the intrinsic cavity Q factor.) Also, smaller resonator with smaller τ_0 produces higher intra-cavity power than larger ones, but the total energy inside the cavity ($|E|^2 \tau_0$) is the same.

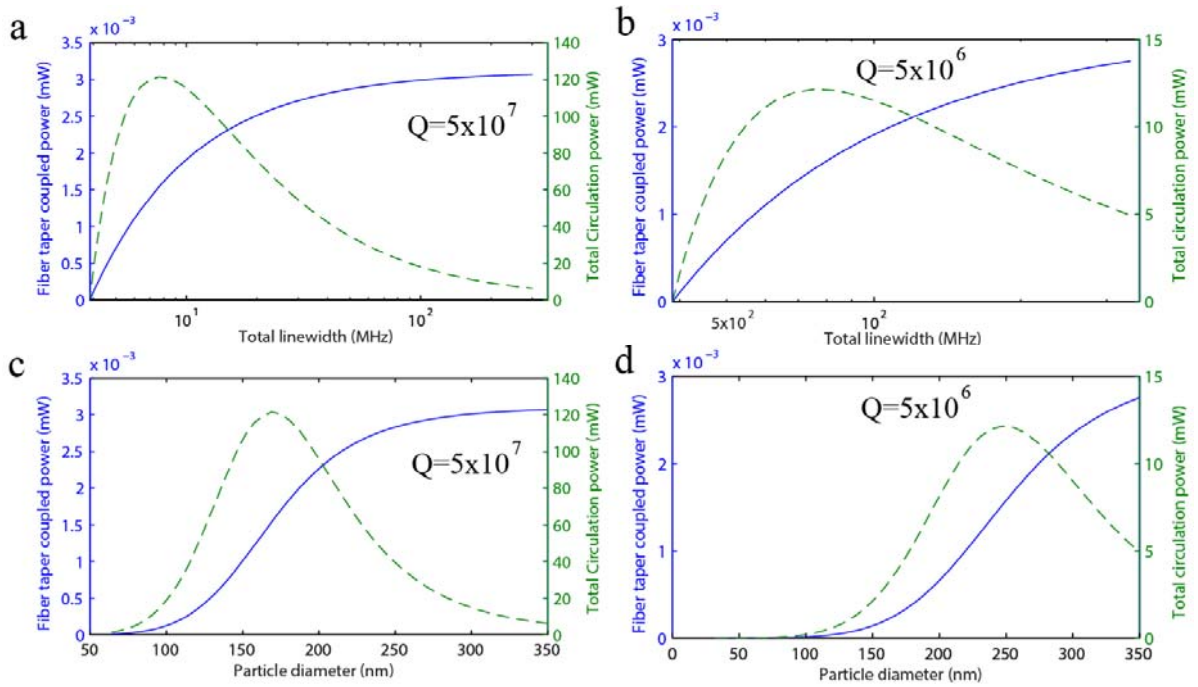
When the fiber taper is present (i.e., fiber taper to extract power from the cavity), we keep fiber taper at critical coupling condition ($\kappa_1 = \kappa_0 + 2\Gamma$), which allows maximum power extraction from the resonator to the fiber taper. Under this condition, when $2\Gamma = \kappa_0$, we obtain the maximum intracavity power as $|E_{cw}|_{\max}^2 = |E_{ccw}|_{\max}^2 = 3\lambda_n^2 I_{in} / (128\pi\tau_0\kappa_0)$. Note that it is 4 times smaller than the case without fiber taper.

The power extracted from fiber taper at critical coupling condition ($\kappa_1 = \kappa_0 + 2\Gamma$) is given by:

$$|a_{fiber}|^2 = |iE_{CW}\sqrt{\tau_0\kappa_1}|^2 = |iE_{sym}\sqrt{\tau_0\kappa_1/2}|^2 = \frac{3\lambda_n^2}{32\pi} \cdot I_{in} \frac{2\Gamma}{\kappa_0 + 2\Gamma} \quad (\text{S14})$$

When the coupling strength of the scatterer is very large or $2\Gamma \gg \kappa_0$ (i.e., $\kappa_1 = 2\Gamma \gg \kappa_0$), we find the maximum power coupled into the fiber taper as $|a_{fiber}|_{\max}^2 = 3\lambda_n^2 I_{in} / 32\pi$, which is not independent of the cavity-specific parameters.

To consider the tradeoff between coupling efficiency and Q degradation, we plot the relation between intracavity power and total linewidth. The change in linewidth was achieved by changing the size of the single particle deposited on the resonator (**Fig. S10**). In **Fig. S10**, we keep the fiber taper at critical coupling ($\kappa_1 = \kappa_0 + 2\Gamma$). It is clearly seen that the intracavity power reaches maximum when the total linewidth is broadened to about twice of the original linewidth. With a high Q resonator ($Q=5 \times 10^7$) and 1mW of free space input light, one can achieve an intracavity power of 122 mW with a fiber taper at critical coupling, or 488mW without the fiber taper, with a single nanoparticle of optimal size. The maximum power coupled into the fiber taper is about 3.1 μ W with a large scatterer ($\kappa_1 = 2\Gamma \gg \kappa_0$). These numbers are consistent (at the same level) with our experimental observation. If one uses the maximum power coupled into the fiber taper as the indication for the efficiency of free space coupling, we find that the coupling efficiency is about 0.31% for a single particle.



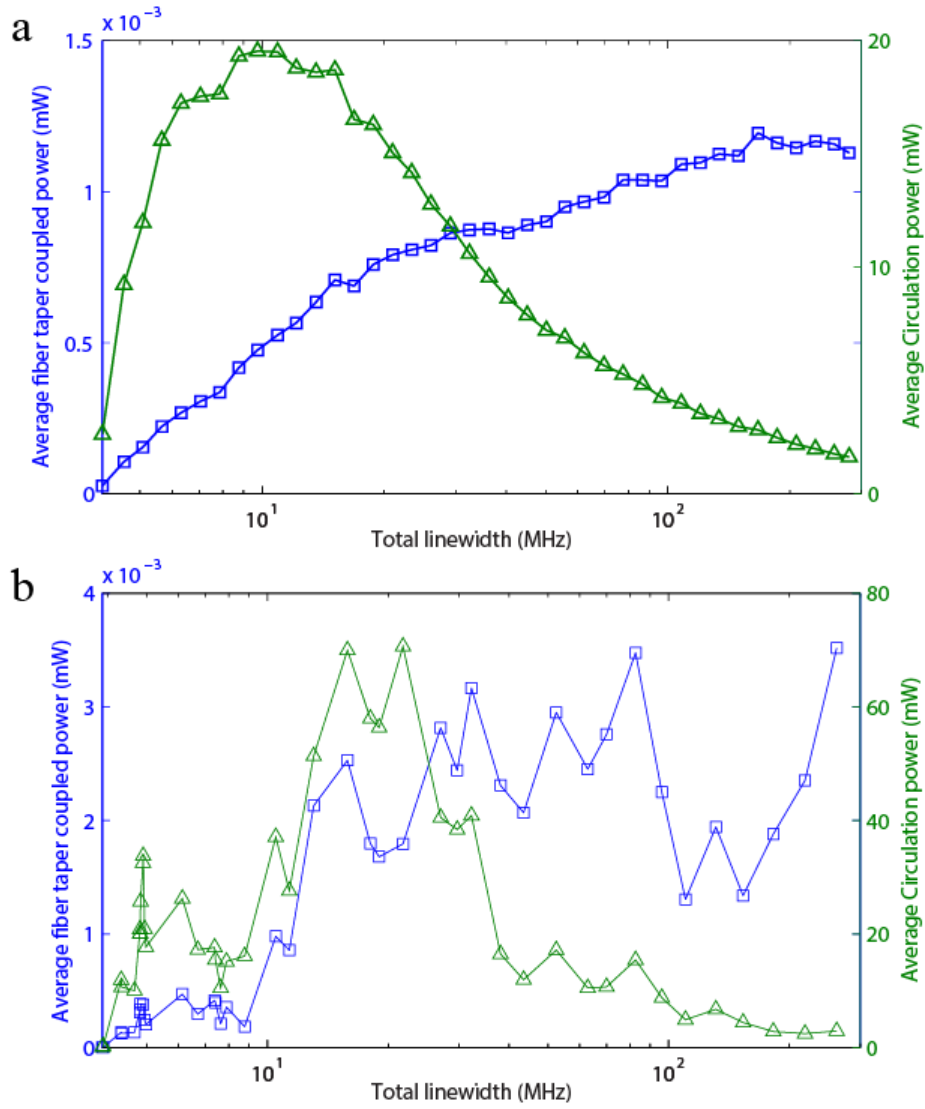
Supplementary Figure S10 | a, b. The relation between the power extracted by the fiber taper and total system linewidth (solid line), and the relation between total intracavity circulation power and total system linewidth (dashed line) for a single spherical nanoparticle. **c, d.** The relation between fiber extracted power and nanoparticle diameter (solid line), and total intracavity circulation power and nanoparticle diameter (dashed line). The refractive index of

the nanoparticle is 1.5, and the normalized overlap between the particle and cavity mode is 0.3. The free space beam spot size is $4\ \mu\text{m}$, with total power of 1 mW. Resonator diameter is $40\ \mu\text{m}$, with intrinsic Q factor of 5×10^7 (a,c) or 5×10^6 (b,d). Wavelength is 1550 nm.

Coupling efficiency and Q degradation with multiple scatterers

To estimate the coupling efficiency and Q degradation as a result of multiple scatterers in the mode volume, we ran simulations according to Eq. (S10-S12). Since in the experiments, nanoparticles were deposited on the resonator surface randomly, we assumed random placement of nanoparticles in the simulations. The results are shown in **Fig. S11**, which are averaged results of 500 simulations. In each simulation, 2000 particles were randomly placed on the resonator. In simulations, the nanoparticles were randomly placed on the resonator, thus, a large portion of the particles are deposited outside of the sensitive area of the resonator ($f(r) < 0.05$), and do not have a significant contribution to the results. We estimate the number of particles that have significant contribution to the coupling of free space light is less than 100. This is also true in experiments, as a large portion of particles are deposited at insensitive area of the resonator and do not affect the experimental results significantly.

As seen in **Fig. S11**, the intracavity power reaches maximum when the total system linewidth is about doubled, corresponding to the critical coupling condition for scatterer-coupling. The power extracted into the fiber taper monotonically increases when the scatterer-induced linewidth broadening is larger. These results are expected and are very similar to the case of a single scatterer (**Fig. S10**). Note that the results in **Fig. S11** are the average of 500 simulations. For each single simulation, there could be significant deviation from the averaged line which manifests as fluctuations, because of the random placement of the particles. We see a good agreement between these results and our experimental results shown in **Fig. 2d** of the main text. The trend is the same despite the fluctuations.



Supplementary Figure S11 | a. The relation between circulation power and total linewidth (line with triangles, and the relation between fiber taper extracted power and total linewidth (line with squares), when multiple particles are placed on a microtoroid. The points are obtained by averaging the results of 500 simulations. In each simulation, 2000 nanoparticles with diameter of 150 nm are randomly deposited on the resonator surface. The free space beam spot diameter is 6 μm , with total power of 1 mW. The resonator in simulation has a diameter of 60 μm , and intrinsic Q factor of 5×10^7 . Wavelength is 1550 nm. The fiber taper is always at critical coupling condition. **b.** Example of individual simulation result showing random fluctuations due to random nanoparticle positions. The result is sampled by 50 points.

Supplementary References

43. Kaplan, A. et al. Finite element simulation of a perturbed axial-symmetric whispering-gallery mode and its use for intensity enhancement with a nanoparticle coupled to a microtoroid. *Optics Express* **21**, 14169-14180 (2013).
44. Tomes, M., Vahala, K.J. & Carmon, T. Direct imaging of tunneling from a potential well. *Optics Express* **17**, 19160-19165 (2009).
45. Liu, Y.C. et al. Cavity-QED treatment of scattering-induced free-space excitation and collection in high-Q whispering-gallery microcavities. *Phys Rev A* **85** (2012).
46. Potton, R.J. Reciprocity in optics. *Rep Prog Phys* **67**, 717-754 (2004).